Gas-phase transport and entropy generation during transient combustion of single biomass particle in varying oxygen and nitrogen atmospheres

Linwei Wang [a], Nader Karimi [1a], Manosh C. Paul [a]
[a] Systems, Power & Energy Research Division, School of Engineering, University of Glasgow, Glasgow G12 8QQ, United Kingdom

Abstract

Transient combustion of a single biomass particle in preheated oxygen and nitrogen atmospheres with varying concentration of oxygen is investigated numerically. The simulations are rigorously validated against the existing experimental data. The unsteady temperature and species concentration fields are calculated in the course of transient burning process and the subsequent diffusion of the combustion products into the surrounding gases. These numerical results are further post processed to reveal the temporal rates of unsteady entropy generation by chemical and transport mechanisms in the gaseous phase of the reactive system. The spatio-temporal evolutions of the temperature, major chemical species including CO, CO_2, O_2, H_2 and H_2O, and also the local entropy generations are presented. It is shown that the homogenous combustion of the products of devolatilisation process dominates the temperature and chemical species fields at low concentrations of oxygen. Yet, by oxygen enriching of the atmosphere the post-ignition heterogeneous reactions become increasingly more influential. Analysis of the total entropy generation shows that the chemical entropy is the most significant source of irreversibility and is generated chiefly by the ignition of volatiles. However, thermal entropy continues to be produced well after termination of the particle life time through diffusion of the hot gases. It also indicates that increasing the molar concentration of oxygen above 21% results in considerable increase in the chemical and thermal entropy generation. Nonetheless, further oxygen enrichment has only modest effects upon the thermodynamic irreversibilities of the system.

Keywords: Biomass; Entropy Generation; Single Particle Combustion; Gaseous Transport; Varying gas-phase atmosphere.

Nomenclature

A	pre-exponential factor, unit vary	$R_{i,cr}$	chemical production rate for species i, $kmol/m^3 \cdot s$
A_p	particle surface area, m^2	s_E	effective area of entropy generation, m^2
$a1, a2, a3$	constants	$\vec{s}$	entropy flux vector
C_D	drag coefficient	s	specific entropy, $J/kmol \cdot K$
c	concentration, $kmol/m^3$	s_b	Stefan-Boltzman constant, $5.67032 \times 10^{-8}\ W/m^2 \cdot K^4$
c_p	specific heat capacity, $J/kg \cdot K$	T	temperature, K
D_{ij}	binary diffusion coefficient for the $i-j$ species pair, m^2/s	T^0	reference temperature, K
$D_{T,i}$	thermal diffusion coefficient for the i^{th} species, m^2/s	t	time, s
D_i	diffusion coefficient of species i, m^2/s	t_t	effective time of entropy generation, s
d	diameter, m	u	velocity, m/s
e	specific internal energy, J	$\vec{u}$	velocity vector
E	entropy generation rate, W/K	$\vec{V_i}$	diffusion velocity of the i^{th} species
E_a	active energy, $J/kmol$	$V_{i,cr}{}'$	stoichiometric coefficients of the reactants of species i in reaction cr

[1] Corresponding author: Nader.Karimi@glasgow.ac.uk

E_h	rate of entropy generation duo to heat transfer, W/K	$V_{i,cr}''$	stoichiometric coefficients of the products of species i in reaction cr
E_m	rate of entropy generation duo to mass transfer, W/K	X	mole fraction
E_r	rate of entropy generation duo to chemical reactions, W/K	Y	mass fraction
E'	average entropy generation rate, W/K		
F_d	drag force, N	*Greek Symbols*	
f_h	fraction of heat absorbed by the particle	α	distribution coefficient of volatile in biomass
$\vec{f_l}$	body force per unit mass	μ	viscosity, $kg/m \cdot s$
$H_{reac_{cr}}$	enthalpy of reaction cr, $J/kmol$	μ_c	specific chemical potential, J/kg
h	specific enthalpy, $J/kmol$	$\overline{\mu_c}$	Molar chemical potential, J/mol
h_{fg}	latent heat of devolatilization, J/kg	μ_m	molecular viscosity, $kg/m \cdot s$
h'	enthalpy of mixture, , $J/kmol$	λ	thermal conductivity, $W/m \cdot K$
g_x	acceleration gravity, m/s^2	ρ	density, kg/m^3
$J_{i,j}$	molecular mass flux, $kg/m^3 \cdot s$	ω_i	rate of species i mass production per unit volume
K	reaction rate, $kmol^{1-(d+e)}/(m^3)^{1-(d+e)} \cdot s$	ε_p	particle emissivity
k_a	rate constant of char combustion reactions, $kmol/m^3 \cdot s$	θ_R	radiation temperature, K
k_c	thermal conductivity, $K \cdot m/W$	σ	Rate of entropy generation per unit volume, W/m^3K
k_{cr}	rate constant of reaction cr, $kmol/m^3 \cdot s$	Φ	viscous dissipation
k_d	kinetic rate of devolatilization reaction, s^{-1}		
Le	Lewis number	*Subscripts*	
M	molecular weight, $kg/kmol$	cr	chemical reaction number
$\overline{M}$	average molecular weight, $kg/kmol$	cr'	char reaction number
m	mass, kg	i	i^{th} species
N	number of chemical species	j	indices: 1,2,…,N
n_{cr}	number of chemical reactions	g	gas
Nu	Nusselt number	p	particle
p	pressure, Pa	rg	gaseous reactants
p^0	reference pressure, Pa	X	composition of chemical element H
Q_r	internal production rate for thermal energy, J/s	Y	composition of chemical element O
q_j	energy flux	x, r	coordinates
$\vec{q}$	heat-flux vector	*Superscripts*	
$\overrightarrow{q_R}$	radiant heat-flux vector	$a_{i,cr}$	reaction order of species i in reaction cr
Re	Reynolds number	b	temperature exponent
Ru	universal gas constant, $kg/kmol$	d	reaction order of related gaseous reactants
R_i	net rate of production of species i due to chemical reactions, $kg/m^3 \cdot s$	e	reaction order of oxygen

Introduction

It is well-established that combustion is, by far, the most irreversible process taking place in thermal power stations [1][2]. Recent studies of coal fired power stations showed that the exergy efficiency of circulating fluidised bed boiler can be lower than 30% [3][4]. This figure clearly reflects the significant role of combustion

process in exergetic losses of thermal power generation. Thus, future improvements in power stations are subject to obtaining a thorough understanding of the irreversibilities of combustion technologies [5]. The recent emphases on low carbon power generation have led to the development of oxy-combustion [6] and a fast growing interest in combustion of biomass [7][8]. Combination of these two technologies along with carbon capture and storage introduces a potential method of negative carbon emissions in power generation [9]. Practical optimisation of oxy-combustion of biomass requires examining the thermodynamic irreversibilities associated with burning of biomass particles in oxygen enriched atmospheres. This, in turn, calls for accurate simulation of biomass combustion in atmospheres with varying concentration of oxygen. Although there exists a large body of literature on oxy-coal combustion (see the reviews in Refs. [6][10]) the equivalent studies for biomass are far less frequent. Given the high complexities of pulverised biomass combustion, analysing combustion of a single biomass particle is expected to better reveal the fundamentals of thermodynamic irreversibilities. Such analysis will be inevitably transient and therefore rather distinctive to the conventional second law studies of reactive flows [11].

The general field of entropy generation in combustion process has already received a considerable attention from the scientific community and the subject has been reviewed by different authors, e.g. [5][11][12]. A vast majority of the literature in this area has focused on entropy generation in combustion of gaseous fuels under premixed or diffusion modes. For conciseness reasons, only those single-phase studies published in the current decade (2010's) are discussed here and readers are referred to Ref. [5] for the review of the earlier works. In a series of numerical studies Chen and co-workers investigated entropy generation on opposing jet combustion of hydrogen and blends of hydrogen and methane in premixed [13][14] and non-premixed [15] modes. Through Lattice-Boltzmann simulations, these authors performed extensive parametric studies and showed that the jet Reynolds number is a key parameter characterising the generation of entropy. In particular, Chen et al. [16] asserted that for low Reynolds number the irreversibility associated with chemical reactions is the dominating source of entropy generation. However, at high Reynolds number the hydrodynamic irreversibilities become more significant. Emadi and Emami [17] analysed the local generation of entropy in a hydrogen-enriched, turbulent non-premixed flame. Their results revealed that, in general, thermal conduction is the most significant source of entropy generation and is followed by that of chemical and mass diffusion processes [17]. However, preheating of air resulted in the reduction of thermal irreversibility and maintained the chemical and mass transfer irreversibilities unchanged. Hence for combustion with preheated air (at above 750K) chemical irreversibilities were reported as the dominant source of entropy generation [17]. On this basis, Emadi and Emami [17] recommended preheating as a means of improving the exergetic efficiency of combustion. More recently, Safer et al. [18] simulated non-premixed combustion of syngas in a counter flow configurations. These authors [18] calculated the rate of entropy generation for different hydrogen contents in the syngas and showed that hydrogen enrichment reduces the irreversibility of the process. Their results also revealed that chemical irreversibilities are the most significant source of entropy generation in the investigated flame configuration [18].

Data collected from direct numerical simulations (DNS) were used by Farran and Chakraborty to evaluate entropy generation in turbulent premixed flames [19]. These authors argued that decreasing the global Lewis number results in increasing thermal, chemical and mass diffusion irreversibilities. Yet, the regime of turbulent premixed combustion was judged insignificant in entropy generation process. Another DNS study of entropy generation in premixed flames revealed that increasing the combustor pressure and the extent of exhaust gas recirculation intensify the rates of irreversibility [20]. It was also shown that for the low Reynolds numbers the

chemical irreversibilities dominate the generation of entropy [20]. Safari and Sheikh [21] conducted a large eddy simulation of entropy generation in turbulent non-premixed jet flames. They found that increases in the turbulence intensity of the jet leads to higher chemical and thermal irreversibilities in the flame [21]. Entropy generation minimisation has been also applied to the design of practical combustors. In a recent study, Arjmandi and Amani [22] simulated the generation of entropy and the second law performance of a swirling bluff-body stabilised flame in a gas turbine combustor. In a parametric study they investigated the influences of equivalence ratio, fuel-inlet flow rate, bluff-body aspect ratio, swirl number, and air-inlet velocity upon the entropy generation and accordingly suggested an optimised deign of the combustor [22].

Entropy generation in single phase combustion has been also extended to microsystems through analysing combustion of mixtures of H_2 and CO [23] and H_2 and CH_4 [24] in microchannel and micro-planar configurations. Multiple step chemical kinetics was employed in these studies, which revealed that the total entropy generation within the system increases by augmenting the inlet velocity of the reactants. They also showed that concentration of CO and H_2 can significantly affect the share of chemical irreversibility in the total entropy generation. The problem of entropy generation in premixed combustion of hydrogen air mixtures in micro-combustors was investigated by Jejurkar and Mishra [25]. This study showed that chemical reactions, heat conduction and mass diffusion are respectively the most important sources of irreversibilities in premixed, micro combustion [25]. It was also demonstrated that combustion irreversibility deceases as the thermal conductivity of the micro-combustor walls increase [25]. In addition to classical premixed and non-premixed combustion modes, entropy generation calculations have been further performed for catalytic partial oxidation of methane [26]. It was shown that chemical irreversibilities dominate the rate of entropy generation in catalytic partial oxidation of methane in a Swiss-roll reactor [26].

Compared to those of single phase, investigations of the second law performance of multiphase combusting flows are much less frequent [5]. In an early theoretical study, Puri examined generation of entropy in droplet combustion [27]. The optimal size of the droplet and velocity of the surrounding medium was calculated in this work [27]. In another pioneering work Dash and Som analysed transient combustion of a single liquid droplet in a convective environment [28]. The unsteady governing equations along with a single step chemical reaction were investigated numerically in this work [28]. It revealed the distribution of temperature and convection coefficients around the circumference of the droplet as well as the history of entropy generation in the course of the burning process [28]. This study was later extended to droplet burning in quiescent atmospheres [29]. It was demonstrated that the initial temperature ratio of the droplet and the atmosphere and also the initial Damköhler number are the key parameters in determining the rate of exergy destruction in droplet combustion [29]. In a more recent numerical investigation, entropy generation was evaluated in quasi-steady combustion of a droplet [30]. It was shown that entropy generation by thermal and chemical mechanism are quite similar [30]. Further, this study indicated that entropy generation rate decreases with increasing ambient temperature and increases with the particle diameter [30]. Gas-phase entropy generation in transient combustion of methanol droplets were examined theoretically and numerically by Pope et al. [31]. Stationary droplet combustion in a low temperature nearly quiescent atmosphere and moving droplet in a preheated atmosphere were investigated [31]. The results showed that entropy generation by chemical reaction increases and entropy generation due to heat and mass transfer reduces by increasing the initial Reynolds number [31]. In keeping with the findings in single phase

combustion flows, Pope et al. [31] showed that comparing to the chemical and thermal irreversibilities, the contribution of mass transfer with the total irreversibility is rather small.

A second law analysis of solid fuel combustion is limited to only few studies on coal and biomass combustion. Som et al. [32] implemented an exergy balance through using the results of a numerical analysis of a pulverised coal tubular combustor. Mondal et al. [33] developed a model of transport phenomena and entropy generation in combustion of a coal particle in quiescent hot gas environment. Due to the stationarity of the particle, spherico-symmetric governing equations were solved in this work. The effects of coal particle diameter, coal composition and the free stream gas phase temperature on temporal variations of process irreversibilities were investigated [33]. The exergetic behaviour of a small scale wood-fired fluidised bed burner under steady state was examined by Baloyi et al. [34]. This study was primarily focused on the influences of air fuel ratio upon the irreversibility of an adiabatic combustor. The authors showed that there is an optimal air fuel ratio, which results in the minimisation of the entropy generation [34].

The preceding survey of literature clearly shows that already there exist in-depth investigations of thermodynamic irreversibilities in single-phase, gaseous combustion. Important conclusions have been made about these systems. For instance, chemical reactions heat conduction and mass diffusion are respectively regarded as the major contributors to entropy generation in premixed flames, while the order of significance is different in non-premixed flames [15][19][20][25]. Further, multiple studies have clarified the effects of preheating and equivalence ratios in gaseous steady combustion [17][22]. Nevertheless, the equivalent studies in multiphase combustion are currently lacking. This is, particularly, the case for transient combustion of solid fuels, which is perhaps due to the complexity of unsteady combustion in burning of solid particles. Further, the rapidly growing importance of biomass combustion and the potential interests in oxy-combustion of biomass for carbon sequestration have warranted second law investigations of biomass combustion.

Further to the significant role of direct biomass combustion in the current and future energy systems, thermochemical conversion of biomass through gasification is becoming a key technology for syngas and hydrogen production [35][36]. In recent years, there has been a rapidly increasing interest in optimising biomass gasifiers, see Ref. [36] for a recent review of literature. Amongst other techniques, exergy and entropy generation minimisation have been employed to improve the design of biomass gasification systems [37]. Central to achieving improved modelling of the second law performance of biomass gasifiers, is obtaining an in-depth understanding of transport and entropy generation during gasification of single particles. However, so far, this has been hindered by the lack of proper numerical and experimental tools. Since gasification and combustion of biomass share a great deal of their fundamentals, numerical simulations developed for combustion can be then extended for the analysis of gasification processes [38][39][40]. Development of such extendable numerical model provides an important motivation for the current work. To achieve these goals, a detailed numerical study is presented for the transient combustion of single biomass particles in preheated O_2/N_2 atmosphere with varying concentration of oxygen. Results of this analysis are subsequently used to investigate different sources of irreversibility in both temporal and spatio-temporal senses.

2. Theoretical and numerical methods

2.1 Problem configuration

The current work includes numerical simulations of the experiment of Khatami et al. [41]. In that work, single biomass particles were released to a cylindrical reactor with constant wall temperate under quiescent and active flow [41]. High speed imaging was used to measure the temperature histories and ignition delay of the biomass particle in the preheated and isothermal surrounding atmosphere. In their experiments, Khatami et al. [41] varied the chemical composition of the gas atmosphere through introducing different blends of oxygen and nitrogen. Here these experiments are simulated. Figure 1 shows the schematic view of the computational domain used in the current study. 2D axisymmetric model was used to conduct the numerical simulations. The particle was released from the top left corner and the domain could include a uniform flow with the same velocity as the experiment. Similar to that in the experiment [41], the walls were maintained at constant temperature.

2.2 Governing equations and assumptions

The operating conditions correspond to those of Refs. [41], and are shown in Table 1. The following assumptions are made throughout this study.

- The biomass particles are assumed to be spherical in shape with nominal diameter of 80 μm [41].
- The gaseous atmosphere is treated as an ideal-gas mixture.

The computational model simultaneously solves the following conservation equations.

The conservation of mass:

$$\frac{\partial \rho}{\partial t}+\frac{\partial}{\partial x}(\rho v_x)+\frac{\partial}{\partial r}(\rho v_r)+\frac{\rho v_r}{r}=0. \tag{1}$$

Conservation of momentum reads,

$$\frac{\partial(\rho v_x)}{\partial t}+\frac{1}{r}\frac{\partial}{\partial x}(r\rho v_x v_r)+\frac{1}{r}\frac{\partial}{\partial r}(r\rho v_x v_r) \tag{2a}$$
$$=-\frac{\partial p}{\partial x}+\frac{1}{r}\frac{\partial}{\partial x}\left[r\mu_m\left(2\frac{\partial v_x}{\partial x}-\frac{2}{3}(\nabla\cdot\vec{v})\right)\right]+\frac{1}{r}\frac{\partial}{\partial r}\left[r\mu_m\left(\frac{\partial v_x}{\partial r}+\frac{\partial v_r}{\partial x}\right)\right]+\rho g_x,$$

$$\frac{\partial(\rho v_r)}{\partial t}+\frac{1}{r}\frac{\partial}{\partial x}(r\rho v_x v_r)+\frac{1}{r}\frac{\partial}{\partial r}(r\rho v_r v_r) \tag{2b}$$
$$=-\frac{\partial p}{\partial r}+\frac{1}{r}\frac{\partial}{\partial x}\left[r\mu_m\left(\frac{\partial v_x}{\partial r}+\frac{\partial v_r}{\partial x}\right)\right]+\frac{1}{r}\frac{\partial}{\partial r}\left[r\mu_m\left(2\frac{\partial v_r}{\partial r}-\frac{2}{3}(\nabla\cdot\vec{v})\right)\right]$$
$$-2\mu_m\frac{v_r}{r^2}+\frac{2}{3}\frac{\mu_m}{r}(\nabla\cdot\vec{v}).$$

Balance of energy for the reactive flow is written as [44] [45],

$$\frac{\partial(\rho h')}{\partial t}+\frac{\partial(\rho h' u_r)}{\partial r}+\frac{\partial(\rho h' u_x)}{\partial x}=\frac{\partial p}{\partial t}-\frac{\partial q_j}{\partial(x,r)}+Q_r, \tag{3a}$$

where

$$q_j=\frac{c_p}{\lambda}\left[-\frac{\partial h}{\partial(x,r)}+\left(1-\frac{1}{Le}\right)\sum\nolimits_i^N h_i\frac{\partial Y_i}{\partial(x,r)}\right], \tag{3b}$$

$$Le=-\frac{\lambda}{\rho c_p D_i}, \tag{3c}$$

and the conservation of species is expressed by

$$\frac{\partial(\rho Y_i)}{\partial t}+\frac{\partial(\rho Y_i u_r)}{\partial r}+\frac{\partial(\rho Y_i u_x)}{\partial x}=\frac{\partial(J_{i,j})}{\partial(x,r)}+R_i, \tag{4a}$$

in which

$$J_{i,j}=-\rho D_i\frac{\partial Y_i}{\partial(x,r)}, \tag{4b}$$

$$R_i=M_i\sum\nolimits_{cr=1}^{n_{cr}}R_{i,cr}, \tag{4c}$$

$$R_{i,cr} = K_{cr}\left(V''_{i,cr} - V'_{i,cr}\right)\prod_{i=1}^{N} c_i^{a_{i,cr}}, \quad (4d)$$

$$K_{cr} = A_{cr}T^{b_{cr}}exp\left(-E_{a,cr}/R_uT\right). \quad (4e)$$

The ideal gas law for the multicomponent gas is written as

$$p = \rho R_u T \sum_i^N \frac{Y_i}{M_i}. \quad (5)$$

The unsteady motion of the biomass particle and energy balance was also included in the computational model. The transient motion of the particle was modelled by considering the gravitational and aerodynamic lift forces through the following equations [42]. The constants a_1, a_2, a_3 are given in Table 2 [43]. It is further noted that the gas viscosity appearing in Eq. 6 is calculated on the basis of an ideal gas mixture.

$$m_p\frac{du_p}{dt} = F_d\left(u_g - u_p\right) + g_x\left(\rho_p - \rho\right), \quad (6a)$$

$$F_d = \frac{3\mu}{\rho_p d_p^2}\frac{C_D Re_p}{4}, \quad (6b)$$

$$Re_p = \frac{\rho d_p\left|u_p - u_g\right|}{\mu_g}, \quad (6c)$$

$$C_D = a_1 + \frac{a_2}{Re_p} + \frac{a_3}{Re_p^2}. \quad (6d)$$

The balance of energy for the particle is given by the following equation, which takes into account convection and radiation heat transfer and also considers phase change of the particle [44][45].

$$m_p c_{p,p}\frac{dT_p}{dt} = \pi d_p \lambda Nu\left(T_g - T_p\right) + A_p\varepsilon_p s_b\left(\theta_R^4 - T_p^4\right) + \frac{dm_p}{dt}h_{fg} - f_h\sum_{cr'}\frac{dm_p}{dt}H_{reac_{cr'}} \quad (7a)$$

in which the Nusselt number is given by the following equation.

$$Nu = 2.0 + 0.6\cdot Re_p^{1/2}\cdot\left(c_p\mu_g/\lambda\right)^{1/3}. \quad (7b)$$

In Eq. 7a the term on the left hand side represents the temporal rate of change in the sensible enthalpy of the particle. Further, the first and second terms on the right hand side show the heat transfer from the particle by the mechanisms of heat convection and radiation. The third term on the right hand side denotes the energy change during particle devolatilisation process. The last term on the right hand side represents the fraction of the enthalpy of heterogeneous reactions that is absorbed by the particle. In Eq. 7a, $\frac{\mathrm{dm_p}}{\mathrm{dt}}$ represents the mass changes during the devolatilisation and char combustion process respectively, which is coupled automatically by the solver (ANSYS Fluent) under DPM model.

2.3 Combustion Model

Table 3 provides a summary of the characteristics of the biomass particle used in the current investigation. Four physicochemical processes were considered during combustion of solid fuel particles. These include devolatilisation of the particle, volatile (represented by CH_xO_y) combustion, char (represented by $C_{(s)}$) oxidation and other gas phase reactions [46]. The particles are heated by the hot surrounding gases and also thermal radiation from the walls and consequently they first release their moisture content (drying process). Then volatiles are released rapidly (devolatilisation process). In this study, the release of volatiles is described by the single rate

model [47]. It is assumed that the rate of devolatilisation is first-order and depends on the amount of volatiles remaining in the particle and employs global kinetics [45]. The reaction and its kinetic rate are:

$$R1: Biomass \rightarrow \alpha\, Volatile + (1-\alpha)\, Char, \quad (8)$$

$$k_d = Aexp(-E_a/R_uT). \quad (9)$$

where α is the distribution coefficient of volatile in biomass. Char formed during devolatilisation process is consumed by heterogeneous processes of combustion and gasification. Its combustion yields carbon monoxide (CO) and carbon dioxide (CO_2). The following heterogeneous reaction are considered here [42][48][49], which include the char-H_2O reaction.

$$R2: C_{(s)} + O_2 \rightarrow CO_2, \quad (10)$$

$$R3: C_{(s)} + 0.5\, O_2 \rightarrow CO, \quad (11)$$

$$R4: C_{(s)} + CO_2 \rightarrow 2\, CO, \quad (12)$$

$$R5: C_{(s)} + H_2O \rightarrow H_2 + CO. \quad (13)$$

Then, the reaction rate K (kmol/m^{3}s) is defined as

$$K = k_a C_{c(s)} C_{rg}, \quad (14)$$

and k_a is the reaction rate constant given by the Arrhenius type relation:

$$k_a = AT^b exp(-E_a/R_uT). \quad (15)$$

Further, C_{rg} is the concentration of the gaseous reactant, which is O_2 for R2 and R3 and CO_2 and H_2O for R4 and R5, respectively. The detailed chemical species in the volatile are not completely understood yet, owing to the complexity of the chemical structure of biomass [50]. It is, therefore, generally treated as a single species which varies depending on the type of coal and comprising carbon, hydrogen and oxygen (CH_xO_y) in a ratio determined from the ultimate analysis of coal and biomass in order to simplify the study [44]. For the biomass bagasse used in this study, the volatile gas species are represented as $CH_{1.89}O_{0.94}$.

The homogeneous reaction related to the volatile is given by

$$R6: CH_XO_Y + m\, O_2 \rightarrow CO_2 + n\, H_2O. \quad (16)$$

Thus, equating the numbers of atoms of each element in the reactants to the number in the products gives: $m = 1 + X/4 - Y/2$, $n = X/2$, and the oxidation of carbon monoxide (CO) [51] and hydrogen (H_2) [52] are according to the following homogeneous reaction.

$$R7: CO + 0.5\, O_2 \rightarrow CO_2, \quad (17)$$

$$R8: H_2 + 0.5\, O_2 \rightarrow H_2O. \quad (18)$$

The reaction rates are given by

$$K = AT^b \exp(-E_a/R_uT)[c_R]^d[c_{ox}]^e. \quad (19)$$

Here c_{rg} is the concentration of CH_XO_Y for R6, CO for R7 and H_2 for R8 respectively. Eight chemical reactions are considered, in total, and a summary of the kinetics data used in the present combustion modelling and the values of d and e are provided in Table 4.

2.4 Numerical scheme

Figure 1 shows the computational grid, which was generated using ICEM. A grid-independency study was carried out and grid densities with 18950, 29925, 37710 and 52680 cells were examined. The simulation results based on the four investigated meshes were very close to each other. Thus, in the current study, the grid with

29925 cells was chosen. The numerical modelling was conducted using an Euler-Lagrange model. The weighted-sum-of-grey-gases model (WSGGM), standard $k-\varepsilon$ was used to model turbulence. Further, P-1 radiation (spherical harmonic method) [53], single kinetic rate de-volatilisation [47] and multiple-surface-reactions combustion model (e.g., char-O_2, char-CO_2, and char-H_2O) [42][48][49] were employed. SIMPLE algorithm was implemented for velocity-pressure coupling and simulations were run in ANSYS FLUENT [42].

2.5 Gas-phase entropy generation

The derivation of entropy generation rate makes use of the governing equations and Gibbs equation [54]. For the completeness of the analysis, the major steps of this derivation are summarised in the followings. The Gibbs equation for a multi-component gaseous mixture reads

$$Tds = de + pd\left(\frac{1}{\rho}\right) - \sum_i \mu_{c,i} dY_i. \tag{20}$$

This equation applies for any differential change in the applicable parameters, therefore one can write,

$$T\frac{\partial s}{\partial t} = \frac{\partial e}{\partial t} - \frac{p}{\rho^2}\frac{\partial \rho}{\partial t} - \sum_i \overline{\mu_{c,i}}\frac{\partial Y_i}{\partial t}, \tag{21}$$

where $\mu_{c,i} = \overline{\mu_{c,i}}/W_i$ is the specific chemical potential.

Substituting the governing equations (1)-(3) into Gibbs equation and multiplying the result by ρ/T renders

$$\rho\frac{\partial s}{\partial t} = -\frac{1}{T}\nabla\cdot\vec{q} + \frac{\Phi}{T} + \frac{\rho}{T}\sum_i Y_i\vec{f_i}\cdot\vec{V_i} - \frac{1}{T}\sum_i \mu_{c,i}\left[\omega_i - \nabla\cdot\left(\rho Y_i\vec{V_i}\right)\right], \tag{22}$$

which can be rewritten as

$$\begin{aligned}\rho\frac{\partial s}{\partial t} = -\nabla\cdot\left[\left(\frac{\vec{q}}{T}\right) - \frac{1}{T}\sum_i \mu_{c,i}\rho Y_i\vec{V_i}\right] - \frac{\vec{q}}{T^2}\cdot\nabla T + \frac{\Phi}{T} + \frac{\rho}{T}\sum_i Y_i\vec{f_i}\cdot\vec{V_i} \\ - \frac{1}{T}\sum_i \mu_{c,i}\omega_i + \frac{1}{T^2}\sum_i \mu_{c,i}\rho Y_i\vec{V_i}\cdot\nabla T - \frac{1}{T}\sum_i \rho Y_i\vec{V_i}\cdot\nabla\left(\mu_{c,i}\right).\end{aligned} \tag{23}$$

By comparing the equation of change for entropy presented by Hirschfelder et al. [55], Eq. (23) leads to the following equations:

$$\vec{s} = \left(\frac{\vec{q}}{T}\right) - \frac{1}{T}\sum_i \mu_{c,i}\rho Y_i\vec{V_i}, \tag{24}$$

and

$$\sigma = -\frac{\vec{q}}{T^2}\cdot\nabla T + \frac{\Phi}{T} + \frac{\rho}{T}\sum_i Y_i\vec{f_i}\cdot\vec{V_i} - \frac{1}{T}\sum_i \mu_{c,i}\omega_i + \frac{1}{T^2}\sum_i\left(\mu_{c,i}\rho Y_i\vec{V_i}\right)\cdot\nabla T - \frac{1}{T}\sum_i \rho Y_i\vec{V_i}\cdot\nabla\left(\mu_{c,i}\right). \tag{25}$$

The preceding equation can be manipulated into a form similar to that given by Carrington and Sun [56]:

$$\sigma = -\frac{\vec{q}}{T^2}\cdot\nabla T + \frac{\Phi}{T} + \frac{1}{T}\sum_i \rho Y_i\vec{V_i}\cdot\left(\vec{f_i} + \frac{\mu_{c,i}}{T}\nabla T - \nabla\mu_{c,i}\right) - \frac{1}{T}\sum_i \mu_{c,i}\omega_i. \tag{26}$$

At any given point, the total heat flux $\vec{q}$ can be defined as follows

$$\vec{q} = \overrightarrow{q'} + \rho\sum Y_i\vec{V_i}h_i, \tag{27}$$

$$\text{where } \overrightarrow{q'} = -\lambda\nabla T + R_u T\sum_i\sum_j\left(\frac{X_j D_{T,i}}{M_i D_{ij}}\right)\left(\vec{V_i} - \vec{V_j}\right) + \overrightarrow{q_R}, \tag{28}$$

and contains the components due to heat conduction, thermal radiation and Dufour effect. It should be noted that the latter is not considered in the current numerical simulations. Thus, the rate of entropy generation reduces to

$$\sigma = -\frac{\vec{q}}{T^2}\cdot\nabla T + \frac{\Phi}{T} + \frac{1}{T}\sum_i \rho Y_i \vec{V_i}\cdot\left(\vec{f_i} + \frac{(\mu_{c,i} - h_i)}{T}\nabla T - \nabla\mu_{c,i}\right) - \frac{1}{T}\sum_i \mu_{c,i}\omega_i. \tag{29}$$

It is then assumed that the gas phase is as an ideal-gas mixture and there exists no external forces. Further, the viscous dissipation contribution is negligible and also pressure and density gradients are small. These render:

$$\mu_{c,i} = h_i - Ts_i, \tag{30}$$

$$s_i = s_i^0 + \int_{T^0}^{T} \frac{c_{p,i}}{T} dT - R_i ln\left(\frac{p}{p^0}\right) - R_i lnX_i, \tag{31}$$

$$\nabla X_i = \sum_{\substack{j=1 \\ j\neq i}}^{N} \left(\frac{X_i X_j}{D_{ij}}\right)(\vec{V_j} - \vec{V_i}) + \sum_{\substack{j=1 \\ j\neq i}}^{N} \left(\frac{X_i X_j}{D_{ij}}\right)\left(\frac{D_{T,j}}{\rho_j} - \frac{D_{T,i}}{\rho_i}\right)\left(\frac{\nabla T}{T}\right). \tag{32}$$

Combining these equations, the rate of entropy generation takes the form of

$$\sigma = \frac{\lambda}{T^2}(\nabla T)^2 + \frac{\rho R_u D_{im}}{\bar{M}}\frac{1}{X_i}(\nabla X_i)^2 + \frac{R_u}{\bar{M}T}\sum_i \frac{D_{T,i}}{Y_i}\nabla T\cdot\nabla X_i - \frac{1}{T}\sum_i \mu_{c,i}\omega_i. \tag{33}$$

The terms on the right-hand side of Eq. (33) represent the rate of entropy generation duo to heat transfer, mass transfer (E_h), heat-mass coupling (E_m) and chemical reactions (E_r), respectively.

$$E_h = \frac{\lambda}{T^2}(\nabla T)^2, \tag{34a}$$

$$E_m = \frac{\rho R_u D_{im}}{\bar{M}}\frac{1}{X_i}(\nabla X_i)^2 + \frac{R_u}{\bar{M}T}\sum_i \frac{D_{T,i}}{Y_i}\nabla T\cdot\nabla X_i, \tag{34b}$$

$$E_r = -\frac{1}{T}\sum_i \mu_{c,i}\omega_i. \tag{34c}$$

Eq. (33) represents the rate of entropy generation per unit volume. Thus the entropy generation rate for the whole system can be found by

$$E = \int \sigma ds_E, \tag{35}$$

in which s_E is the effective area of entropy generation and the average entropy generation over the entire course of burning process is given by the following relation,

$$E' = \frac{1}{t_t}\int_0^{t_t} E dt. \tag{36}$$

The flow data required for entropy generation calculations were extracted from the CFD solver and then post-processed in MATLAB.

3. Results and discussion

3.1 Validation

Figure 2 illustrates a comparison between the current numerical simulations and the experimental measurements of Khatami et al. [41] for varying concentrations of oxygen. This includes the ignition delay (Fig. 2a), the maximum temperature encountered during the transient combustion of biomass particle (Fig. 2b) and the particle life time (Fig. 2c). It should be noted that following Refs. [41][57][58], the ignition delay time accounts

for the duration that was commenced with the biomass particle releasing into the drop furnace and terminated at the ignition moment. Particle life time shows the time taken from the biomass particle releasing to the extinction of the particle. Further, particle maximum temperature is the highest temperature of the particle encountered during the course of transient combustion process. In the experimental studies, spectral measurement was used to monitor the whole combustion process. The start and end points of the particle combustion were determined by the appearance and disappearance of the light emitted from the reactive particle, and the temperature was obtained through signals post-processing [59][60]. In accordance with this methodology, in the simulations the ignition and extinction moments of the particle were deduced by the start and end points of char combustion reactions ($R2-R5$). Further, the temperature of the particle was tracked under the discrete phase modelling (DPM).

In Fig.2, the existence of a close agreement between the simulated and measured data is evident. Further, although not shown in here, the outputs of the numerical model were compared against the experimental data reported in Refs. [41][57][58]. In total, 81 data points were used for comparison, all resulting in excellent agreement with the simulations. Given these, the numerical model is deemed validated.

3.2 Spatio-temporal evolution of the temperature and concentration fields

Figure 3 shows the calculated history of mass loss of the particle (Fig. 3a) and its temporal location (Fig. 3b) under different concentrations of oxygen. It is clear from Fig. 3a that, the inflection points of the curves divide the whole process of particle combustion into two stages: devolatilisation stage and char combustion stage. The mass loss of the particle within the first few milliseconds is quite significant, which corresponds to devolatilisation stage prior to the particle ignition. Over this stage large molecules are decomposed to lighter gas phase matter and are released to the surrounding atmosphere. Figure 3a further shows that ignition of the particle majorly impedes the rate of mass loss and for all investigated oxygen concentrations the char burning lose mass much slower than the devolatilising ones. Increasing the concentration of oxygen accelerates the combustion process and hence the rate of mass loss. However, regardless of the composition of the surrounding atmosphere, most the particle mass is lost during the devolatilisation stage. This is to be anticipated as the proximate analysis, shown in Table 3, indicates that more than 80% of the particle mass consists of volatiles. Figure 3b indicates that the particle kinematics are highly affected by the mass loss. As expected, over the early stage of the particle release it accelerates downward. Yet, Fig. 3b shows that the acceleration decreases significantly towards the end of the particle life time. This is due to the mass loss of the particle, which has progressively increased the relative significance of aerodynamic drag forces in comparison with the gravitational forces. Thus, the particle motion has become quite slow just before the completion of transient combustion process.

Figure 4 depicts the temperature field within the near particle region, specified in Fig. 1, and for different moments after release of the particle. In Fig. 4a, the mole fraction of oxygen is 37%. The first part of this figure (the left most subfigure) corresponds to 3ms after the release of the particle, which is prior to ignition. As expected, the fluid flow, for almost the entire domain, is isothermal and at 1200K. An exception to this is a small area very close to the particle. Due to the endothermic devolatilisation process, the temperature has dropped to around 1100K in the vicinity of the particle. After 5ms the particle has already ignited and passed its peak temperature, the location of the particle and the reactive gas around it are completely clear in the second subfigure of Fig. 4a. The subsequent two subfigures correspond to the final stage of combustion in which the particle becomes exceedingly small and the temperature of the reactive region has decreased. The same qualitative behaviour is observed in Fig. 4b for oxygen mole fraction of 77%. In this figure, the temperature of the burning particle after

6ms is 2000K. This is subsequent to the ignition and occurrence of the peak temperature. The particle and flow temperature drop significantly towards the end of the particle life time. Figure 4b also shows the temperature of the domain after the completion of the transient burning process. Importantly, the none-reactive flow at this stage still features significant temperature gradients. As will be discussed later, this has major influences upon the transient irreversibilities of the process.

Spatio-temporal distributions of different chemical species have been shown in Figs. 5-8 for oxygen mole fraction of 21% and 77%. Figure 5a depicts the evolution of CO under 21% molar concentration of oxygen, a small cloud of CO appears around the particle shortly after the ignition. As the process continues, the amount of CO increases as a result of the progress in R3 and R4 reactions. This is represented by the growth of the cloud of CO around the particle. However, at the end of the particle life time (t=21ms), the concentration of CO drops to zero. This is due to the conversion of CO to CO_2 by reaction R7 and is an indication of the completion of the combustion process. For 77% O_2 molar concentration, Fig. 5b shows that no CO is generated prior to ignition of the biomass particle and similar to that observed in Fig. 5a, after the transient burning there is no CO left in the gas atmosphere. It should be noted that as the legend of Fig. 5b indicates the concentration of CO in oxygen enriched atmosphere is higher compared to that with 21% of oxygen mole fraction.

Figure 6 shows the spatio-temporal distribution of CO_2 for the two considered concentrations of oxygen. Formation of a large amount of CO_2 shortly after the ignition is evident in Fig. 6a. This is due to the oxidisation of the volatiles, as denoted by the homogenous reaction R6. The subsequent production of carbon dioxide in the vicinity of the particle by reactions R2 and R7 is clear in other subfigures of Fig. 6a. These subfigures also show the initial cloud of CO_2 diffuses out and is partially advected downstream. Notably, it is inferred from Fig. 6a that the production of carbon dioxide occurs chiefly by homogenous reactions almost immediately after ignition. This finding will be further verified later. At higher mole fraction of oxygen, shown in Fig. 6b, the qualitative trend of carbon dioxide generation remains largely unchanged. No CO_2 is observed prior to the ignition and the post-ignition plume of CO_2 is advected and diffuses during the transient burning process. However, a comparison between Figs. 6a and 6b reveals that under 77% oxygen mole fraction and for the entire combustion process, the highest concentration of CO_2 within the reactor is situated close to the particle. This is clearly not the case in Fig. 6a in which the CO_2 concentration around the burning particle is considerably smaller than that produced by combustion of devolatilisation gases. The disparity can be attributed to the intensification of reaction R2 and also R3 + R7 due to higher oxygen concentration.

Hydrogen production by steam gasification reaction (or water gas reaction) R5 is depicted in Fig. 7. In Fig. 7a and for 21% mole fraction of oxygen, the formation of hydrogen continues for the first three demonstrated snapshots. However, after 17ms the amount of hydrogen has decreased and it has completely disappeared by the end of the particle life time. This is because of the oxidation of hydrogen to water vapour by reactions R8. A similar trend is observed in Fig. 7b and below 77% mole fraction of oxygen, wherein hydrogen is produced throughout most of the burning process but is ultimately totally converted to water. Yet, the transient concentrations of hydrogen in Fig.7b are significantly higher than those of Fig. 7a. This increase could be attributed to two factors of higher temperature of the gas and water vapour concentration in the vicinity of the burning biomass particle. Hotter gas favours the progress of endothermic water gas reaction and boosts hydrogen production through reaction R5. At the same time, the added hydrogen results in generation of more water vapour by reaction R8, which in turn intensifies reactions R5 and results in depletion of hydrogen. Another contributor

to hydrogen production at higher oxygen concentrations is reaction R6 in which high oxygen concentration leads to fast generation of water vapour and hence accelerates reaction R5.

Production of water vapour has been investigated in further details in Fig. 8. As a consequence of reaction R6, gas phase combustion of volatile matters results in the generation of a large amount of water vapour in the early stages of the transient combustion. This can be clearly seen in Fig. 8a (for 21% of oxygen mole fraction). Further, at the higher oxygen concentration case, shown in Fig. 8b, there is no water vapour prior to ignition, while ignition of the particle generates a dense cloud of water vapour. In both low and high oxygen cases, the water vapour cloud diffuses towards the surrounding gases and at the same time is advected downstream. This behaviour can be clearly seen in Fig. 8a. Nonetheless, the downstream motion of the water vapour cloud is less noticeable in Fig. 8b. This could to be related to buoyancy effects, water molecules are lighter than the average molecular weight of the atmosphere in both investigated cases. However, by increasing the concentration of oxygen the molecular weight of the gaseous atmosphere increases and hence the buoyancy forces acting on the water vapour cloud is magnified. This effect tends to maintain most of the generated water vapour at the top section of the reactor in Fig. 8b.

Figure 9 shows the radial distribution of the mass fraction of oxygen for selected instances of time after releasing the particle. Each graph shows the variations in the mass fraction of oxygen along a radius that initiates from the external surface of the particle and penetrates for 1mm into the surrounding gases. All four different concentrations of oxygen have been investigated in Fig. 9. For the lowest concentration of oxygen in Fig. 9a, oxygen mass fraction in the vicinity of the particle drops at the moment of ignition (3ms) and continues to decrease for the first 6ms before it rises again in the rest of the burning process. This figure shows that particle combustion can affect oxygen concentration of the surrounding gas for a maximum radial distance of about $400\mu m$ from the external surface of the particle. Increasing the concentration of oxygen in Figs. 9b, 9c and 9d results in the following changes. First, the radial extent of oxygen depletion extends significantly. For instance, Fig. 9b shows that under 37% mole fraction of oxygen burning can influence the concentration of oxygen up to 800 μm away from the surface. Second, the decrease in the mass fraction of oxygen becomes a lot more pronounced. Figure 9c, for instance, shows that mass fraction of oxygen drops from nearly 0.8 far from the particle to almost 0.3 on the surface of the particle. However, this value is considerably smaller in Fig. 9a. Given that the mass of particle and hence the total amount of fuel is fixed in all investigated cases, this result may seem counterintuitive. However, it should be recalled that combustion duration becomes significantly faster under oxygen enriched atmospheres (see Fig. 2). Hence, although the total amount of oxygen for complete oxidation of the fuel particle is unchanged, the rate of oxygen consumption in Figs. 9b, 9c and 9d is generally higher than that in Fig. 9a.

Figure 10 shows the temporal evolution of the major chemical species for two different values of oxygen mole fraction in the gaseous atmosphere. The very fast release of volatile matters within the first few milliseconds of the process is clear in both Figs. 10a and 10b. Ignition is marked by the onset of CO_2 and H_2O formation, which expectedly coincides with the peak point in the volatile formation curve. Immediately after ignition, the concentration of volatiles drops sharply, while those of CO_2 and H_2O increase quickly. Figures 10a and 10b shows that in both cases the rate of formation of water vapour and carbon dioxide are almost exactly the same for the post ignition period. Nonetheless, for pure oxygen atmosphere, shown in Fig. 10b, the rate of CO_2 formation exceeds that of H_2O after about 1ms. In both Figs. 10a and 10b formation of CO_2 and H_2O occurs most rapidly while the products of volatilisation are burning and hence the mole fraction of volatiles is non-zero. As soon as

the volatiles are totally consumed and the chemical system becomes largely heterogeneous, the rate of CO_2 formation decreases noticeably. Further, the concentration of H_2O starts to decrease, which is due to the consumption of H_2O by reaction R5. It should be noted that as Fig. 10 depicts, concentration of H_2 remains negligibly small during the entire burning process and therefore the water generation by oxidation of hydrogen is a minor contributor to the total H_2O mole fraction. Formation of carbon monoxide starts just before the end of volatile burning process and increase towards a maximum value and reduces to zero at the end of the particle life time. The reduction of CO life span in pure oxygen (Fig. 10b) in comparison with air (Fig. 10a) is completely clear in this figure.

3.3 Entropy generation

Figures 11 and 12 demonstrate the spatio-temporal evolution of local entropy generation. The thermodynamic irreversibility of the process has been divided into three sources of thermal, mass transfer and chemical reactions as described by Eqs. 34. Figures 11 and 12 show the spatial distribution of entropy generation by each of these sources for selected instances of time and oxygen concentrations in the atmosphere. The horizontal axes of the subfigures in these two figures show the radial distance from the reactor centreline and the vertical axes represent the downward vertical distance from the particle releasing point.

Figure 11 shows that for $\mathrm{t} = 2\mathrm{ms}$, which corresponds to pre-ignition period, there exist some thermal entropy generation due to the endothermic devolatilisation process. Diffusion of the produced gases at this stage has resulted in mass transfer irreversibilities, while entropy generation by chemical reactions is zero. Thus, for pre-ignition stage the mass transfer irreversibility is the dominant source of entropy generation. After 6ms (the middle column in Fig. 11) the combustion process of the particle has progressed to some extent. It is clear that the region over which thermal entropy is generated has increased significantly, while the order of magnitude of this irreversibility has remained unchanged in comparison with the pre-ignition period. The spatial distribution of thermal irreversibility (Fig. 10d) further shows that there are two sources of thermal entropy generation. One situated close to the top of the reactor where volatiles have been released and reacted and the other one is around the burning particle. A comparison between Figs. 11b and 11e indicates that the reactor region affected by mass transfer has slightly decreased during the process. This is mainly due to the fact that volatile release and combustion are limited to a short time after release of the particle. Figures 4 to 8 showed the mass transfer of species generated after completion of volatile combustion is rather slow. This results in weakening of the mass transfer irreversibility, as depicted by Fig. 11e. Figure 11f illustrates the distribution of reaction irreversibilities at $\mathrm{t} = 6\mathrm{ms}$. It is important to note that, in this figure, the entropy generation is stronger than those in Figs. 11e and 11d by an order of magnitude. Further, the regions over which chemical entropy is generated are large and comparable to those affected by thermal entropy (shown in Fig. 11d). Furthermore, generation of chemical entropy is clearly divided into two regions corresponding to the reaction of volatilised gases and the homogenous and heterogeneous reactions in the vicinity of the particle.

As indicated by Fig. 2 for the condition shown in Fig.11 the particle life time is almost 11 milliseconds. Figures 11g, 11h and 11k show the distribution of irreversibilities after 20ms when the burning process has terminated but the resultant heat and species continue to diffusive and generate entropy. Compared to other subfigures, Figs. 11g, 11h and 11k show a larger area of the reactor. Most notably, compared to the earlier time at $\mathrm{t} = 20\,\mathrm{ms}$ the numerical values of all sources of entropy generation have decreased massively. This is

particularly the case for chemical entropy, shown in Fig.11k, which is essentially zero. Figures 11g and 11h show that after completion of combustion the thermal and mass transfer irreversibilities, although smaller in value, cover a much larger area of the reactor compared to the earlier times. Increasing the molar concentration of oxygen to 77% in Fig. 12 results in no qualitative changes in the spatio-temporal evolution of irreversibilities. However, for t=6ms the magnitudes of all sources of entropy generation increased by one order of magnitude in comparison with those in the corresponding subfigures in Fig.11. It also shows that at higher oxygen concentration, chemical and thermal entropy generations are stronger in the near particle region. This is distinctive to that shown in Fig. 11 wherein the upstream reaction of the volatilisation products and the near particle chemical activities contribute almost equally to the thermal and chemical entropy generation.

Figure 13 shows the temporal variation of the three sources of irreversibilities integrated over the entire volume of the reactor. Figures 13a and 13b illustrate the history of entropy generation by the thermal, mass transfer and chemical mechanisms for the particle combustion in an atmosphere with 37% mole fraction of oxygen. This figure reflects a few important points about the transient entropy generation. First, during the life time of the particle the chemical entropy is at least one order of magnitude greater than the heat and mass transfer irreversibilities. Second, the maximum chemical and thermal entropy generations, and hence the maximum total entropy generation, occur at around the ignition time. Both chemical and thermal entropy generations drop sharply after the ignition. Chemical entropy vanishes after the completion of the transient burning process. However, the thermal entropy goes up and continues to grow till the end of the investigated period (100ms). This is due to the diffusion of heat of combustion into the environment after the completion of the transient combustion process. Third, the irreversibility of mass transfer includes two peaks during the particle life time. The first peak corresponds to devolatilisation period and is associated with a local peak in thermal entropy and the second peak happens shortly after the ignition. This represents the entropy generation due to the diffusion of the chemical species generated by the combustion of volatilised gases. Increasing the concentration of oxygen in Figs. 13c and 13d does not change the qualitative (and to a large extend the quantitative) behaviours observed in Figs. 13a and 13b.

The thermal, mass transfer and chemical as well as the total entropy generated during 200 milliseconds after the drop of the particle have been shown in Fig.14. This figure clearly shows the chemical entropy is the most significant contributor with the irreversibility of the process. The thermal entropy has a value of the same order of magnitude as chemical entropy but roughly about three times smaller than that. The mass transfer irreversibility is much smaller than the chemical and thermal entropy generation and can be practically ignored. Figure 14 further shows that increasing the molar concentration of oxygen from 21% results in a considerable increase in thermal and chemical entropy generation and thus significantly intensifies the total entropy generation. Nonetheless, any further increase in the oxygen concentration alters the irreversibilities very slightly.

4. Conclusions

Transient combustion of single biomass particle burning inside a drop-tube furnace and within an oxygen/nitrogen atmosphere was simulated numerically. The investigated cases included four different molar concentrations of oxygen with a slow downward flow. The numerical simulations were compared favourably against the existing experimental results for the maximum particle temperature, ignition delay and particle life time. The results were then used to calculate the spatio-temporal evolutions of the temperature and major chemical

species for the duration of combustion and beyond. Further, the unsteady local entropy fields generated by thermal, mass transfer and chemical irreversibilities inside the reactor were reconstructed. This was integrated over time to predict the total entropy generation. The major findings of this study can be summarised as follows.

- Homogeneous combustion of devolatilised gases tends to dominate the temperature and chemical species concentration at the lowest concentration of oxygen (21% molar basis).
- For higher oxygen concentrations (37%, 77% and 100%) the post combustion homogenous and heterogeneous reactions become increasingly more influential upon the temperature and species concentration fields.
- During pre-ignition period the mass transfer irreversibility is the main source of entropy generation with some contributions from thermal entropy.
- Ignition of the devolatilised gases is the main source of chemical irreversibility and also generates significant thermal irreversibilities.
- Thermal entropy continues to be generated after the termination of the particle life time through diffusion of hot gases into the surroundings.
- Increasing the molar oxygen concentration above 21% results in a sizeable increase in the thermal and chemical entropy generation. However, entropy generations for the higher concentrations of oxygen can be considered nearly constant.
- Overall, the chemical entropy appears to be the dominant source of irreversibility in the problem. The thermal entropy is the second contributor with a similar order of the magnitude as that of chemical entropy and mass transfer irreversibility has a negligibly small contribution.

It is finally noted that, with minimal modifications, the numerical model developed in this work is applicable to the gasification of biomass particles [38, 40].

Acknowledgment

Linwei Wang acknowledges the financial support of Chinese Scholarship Council and the University of Glasgow through a PhD scholarship. N. Karimi acknowledges the financial support by EPSRC through grant number EP/N020472/1 (Therma-pump).

References

[1] Kaushik SC, Reddy SV, Tyagi SK. "Energy and exergy analyses of thermal power plants: A review." Renewable and Sustainable Energy Reviews, 2011, 15(4):1857-1872.

[2] Sciacovelli A, Verda V, Sciubba E. "Entropy generation analysis as a design tool—A review." Renewable and Sustainable Energy Reviews, 2015, 43:1167-1181.

[3] Mert, G, Oztop HF. "Exergy analysis of a circulating fluidized bed boiler cogeneration power plant." Energy Conversion and Management, 2016, 120:346-357.

[4] Regulagadda, P, Dincer I, Naterer GF. "Exergy analysis of a thermal power plant with measured boiler and turbine losses." Applied Thermal Engineering, 2010, 30(80):970-976.

[5] Som SK, Datta A. "Thermodynamic irreversibilities and exergy balance in combustion processes." Progress in Energy and Combustion Science, 2008, 34(3):351-376.

[6] Scheffknecht G, Al-Makhadmeh L, Schnell U, Maier J. "Oxy-fuel coal combustion—A review of the current state-of-the-art." International Journal of Greenhouse Gas Control, 2011, 5:S16-S35.

[7] Koppejan J, Loo SV. The handbook of biomass combustion and co-firing. Routledge, 2012.

[8] Khan AA, Jong WD, Jansens PJ, Spliethoff H. "Biomass combustion in fluidized bed boilers: potential problems and remedies." Fuel Processing Technology, 2009, 90(1):21-50.

[9] Riaza J, Gil MV, Álvarez L, Pevida C, Pis JJ, Rubiera F. "Oxy-fuel combustion of coal and biomass blends." Energy, 2012, 41(1):429-435.

[10] Chen L, Yong SZ, Ghoniem AF. "Oxy-fuel combustion of pulverized coal: characterization, fundamentals, stabilization and CFD modeling." Progress in Energy and Combustion Science, 2012, 38(2): 156-214.

[11] Arpaci VS, Selamet A. "Entropy production in flames." Combustion and Flame, 1988, 73(3): 251-259.

[12] Nishida K, Takagi T, Kinoshita S. "Analysis of entropy generation and exergy loss during combustion." Proceedings of the Combustion Institute, 2002, 29(1):869-874.

[13] Chen S. "Analysis of entropy generation in counter-flow premixed hydrogen–air combustion." International Journal of Hydrogen Energy, 2010, 35(3):1401-1411.

[14] Chen S, Li J, Han H, Liu Z, Zheng C. "Effects of hydrogen addition on entropy generation in ultra-lean counter-flow methane-air premixed combustion." International Journal of Hydrogen Energy, 2010, 35(8):3891-3902.

[15] Chen S, Liu Z, Liu J, Li J, Wang L, Zheng C. "Analysis of entropy generation in hydrogen-enriched ultra-lean counter-flow methane–air non-premixed combustion." International Journal of Hydrogen Energy, 2010, 35(22):12491-12501.

[16] Chen S, Han H, Liu Z, Zheng C. "Analysis of entropy generation in non-premixed hydrogen versus heated air counter-flow combustion." International Journal of Hydrogen Energy, 2010, 35(10):4736-4746.

[17] Emadi A, Emami MD. "Analysis of entropy generation in a hydrogen-enriched turbulent non-premixed flame." International Journal of Hydrogen Energy, 2013, 38(14):5961-5973.

[18] Safer K, Ahmed O, Fouzi T. "Entropy generation in turbulent syngas counter-flow diffusion flames." International Journal of Hydrogen Energy, 2017, 42(49):29532-29544.

[19] Farran R, Chakraborty N. "A direct numerical simulation-based analysis of entropy generation in turbulent premixed flames." Entropy, 2013, 15(5):1540-1566.

[20] Borghesi G, Bellan J. "Irreversible entropy production rate in high-pressure turbulent reactive flows." Proceedings of the Combustion Institute, 2015, 35(2):1537-1547.

[21] Safari M, Sheikhi M. "Large eddy simulation-based analysis of entropy generation in a turbulent nonpremixed flame." Energy, 2014, (15):451-457.

[22] Arjmandi HR, Amani E. "A numerical investigation of the entropy generation in and thermodynamic optimization of a combustion chamber." Energy, 2015, (81):706-718.

[23] Wang W, Zuo Z, Liu J, Yang W. "Entropy generation analysis of fuel premixed CH 4/H 2/air flames using multistep kinetics." International Journal of Hydrogen Energy, 2016, 41(45): 20744-20752.

[24] Jiang D, Yang W, Teng J. "Entropy generation analysis of fuel lean premixed CO/H 2/air flames." International Journal of Hydrogen Energy, 2015, 40(15): 5210-5220.

[25] Jejurkar SY, Mishra DP. "Effects of wall thermal conductivity on entropy generation and exergy losses in a H_2-air premixed flame microcombustor." International Journal of Hydrogen Energy, 2011, 36(24):15851-15859.

[26] Chen WH, Cheng YC, Hung CI. "Entropy generation from hydrogen production of catalytic partial oxidation of methane with excess enthalpy recovery." International Journal of Hydrogen Energy, 2012, 37(19):14167-14177.

[27] Puri IK. "Second law analysis of convective droplet burning." International Journal of Heat and Mass Transfer, 1992, 35(10):2571-2578.
[28] Dash SK, Som SK. "Transport processes and associated irreversibilities in droplet combustion in a convective medium." International Journal of Energy Research, 1991, 15(7):603-619.
[29] Hiwase SD, Datta A, Som SK. "Entropy balance and exergy analysis of the process of droplet combustion." Journal of Physics D: Applied Physics, 1998, 31(13):1601-1610.
[30] Raghavan V, Gogos G, Babu V, Sundararajan T. "Entropy generation during the quasi-steady burning of spherical fuel particles." International Journal of Thermal Sciences, 2007, 46(6):589-604.
[31] Pope DN, Raghavan V, Gogos G. "Gas-phase entropy generation during transient methanol droplet combustion." International Journal of Thermal Sciences, 2010, 49(7):1288-1302.
[32] Som SK, Mondal SS, Dash SK. "Energy and exergy balance in the process of pulverized coal combustion in a tubular combustor." Journal of Heat Transfer, 2005, 127(12):1322-1333.
[33] Mondal, SS. "Modelling of transport processes and associated thermodynamic irreversibilities in ignition and combustion of a pulverized coal particle." International Journal of Thermal Sciences, 2008, 47(11):1442-1453.
[34] Baloyi J, Bello-Ochende T, Meyer JP. "Thermodynamic optimisation and computational analysis of irreversibilities in a small-scale wood-fired circulating fluidised bed adiabatic combustor." Energy, 2014, 70:653-663.
[35] Hossain MA, Jewaratnam J, Ganesan P. "Prospect of hydrogen production from oil palm biomass by thermochemical process–A review." International Journal of Hydrogen Energy, 2016, 41(38):16637-16655.
[36] Ibrahim D, Acar C. "Innovation in hydrogen production." International Journal of Hydrogen Energy, 2017, 42(22):14843-14864.
[37] Rashidi H, Khorshidi J. "Exergy analysis and multiobjective optimization of a biomass gasification based multigeneration system." International Journal of Hydrogen Energy, 2018, 43(5):2631-2644.
[38] Sutardi T, Paul MC, Karimi N, Younger PL. "Numerical Study of the Effects of CO_2 Addition in Single Coal Particle Gasification", Energy Procedia, 2017, 1421:306-1311.
[39] Sutardi T, Paul MC, Karimi N, Younger PL. "Numerical Modelling for Process Investiga-tion of a Single Coal Particle Combustion and Gasification", Proc. of the World Congress on Engi-neering 2017 Vol II: 946-951. 5-7 July, 2017, London.
[40] Salem AM, Kumar U, Izaharuddin AN, Dhami H, Sutardi T, PaulMC. "Advanced Numerical Methods for the Assessment of Integrated Gasification and CHP Generation Technologies", In: De, S. (ed) Coal and Biomass Gasification:307-330, Springer, 2018.
[41] Khatami R, Stiver C, Joshi K, Levendis YA, Sarofim AF. "Combustion behaviour of single particles from three different coal ranks and from sugar cane bagasse in O_2/N_2 and O_2/CO_2 atmospheres." Combustion and Flame, 2012, 159:1253-1271.
[42] ANSYS Fluent Theory Guide 15.0. 2013.
[43] Morsi SA, Alexander AJ. "An investigation of particle trajectories in two-phase flow systems." Journal of Fluid Mechanics, 1972, 55(2):193-208.
[44] Blaid S. Ph.D. thesis. Numerical investigation of the combustion processes of various fuels. University of Glasgow, 2015.
[45] Blaid S, Paul MC, Watson IA. "Numerical investigation of the heterogeneous combustion processes of solid fuels." Fuel, 2015, 141:236–249.
[46] Rosendahl L. Biomass combustion science, technology and engineering. Woodhead Publishing Limited, Cambridge, 2013.
[47] Badzioch S, Hawksley PGW. "Kinetics of thermal decomposition of pulverized coal particles." Industrial & Engineering Chemistry Process Design and Development, 1970, 9(4):521-530.
[48] Chen X, Horio M, Kojima T. "Numerical simulation of entrained flow coal gasifiers. Part I: modeling of coal gasification in an entrained flow gasifier." Chemical Energy Science, 2000, 55: 3861-3874.
[49] Mayers AM. "The rate of reduction of carbon dioxide by graphite." Journal of the American Chemical Society, 1934, 56:70-76.
[50] Jenkinsa BM, Baxterb LL, Miles TR. "Combustion properties of biomass." Fuel Processing Technology, 1998, 54(1-3):17-46.
[51] Howard JB, Williams GC, Fine DH. "Kinetics of carbon monoxide oxidation in postflame gases." Proceedings of 14th Symposium (International) on Combustion, 1973: 975-986.
[52] Serio MA, Hamblen DG, Markham JR, Solomon PR. "Kinetics of volatile product evolution in coal pyrolysis: experiment and theory." Energy & Fuels, 1987, 1:138-152.

[53] Hurt RH. “Structure, properties and reactivity of solids fuels.” In: 27th Symposium (International) on Combustion, The Combustion Institute, 1998: 2887-2904.
[54] Williams FA. Combustion Theory, second ed. Benjamin/Cummings, Menlo Park, California, 1985.
[55] Hirschfelder JO, Curtiss CF, Bird RB. Molecular Theory of Gases and Liquids. Wiley, New York, 1954.
[56] Carrington CG, Sun ZF. Second law analysis of combined heat and mass transfer phenomena. International Journal of Heat and Mass Transfer, 1991, 34(11):2767-2773.
[57] Khatami R, Strivers C, Levendis Y.A. “Ignition characteristics of single coal particles from three different ranks in O_2/N_2 and O_2/CO_2 atmospheres.” Combustion and Flame, 2012, 159:3554-3568.
[58] Maffei T, Khatami R, Pierucci S, Faravelli T, Ranzi E, Levendis YA. “Experimental and modeling study of single coal particle combustion in O_2/N_2 and Oxy-fuel (O_2/CO_2) atmospheres.” Combustion and Flame, 2013, 160:2559-2572.
[59] Levendis YA, Estrada KR. “Development of multicolour pyrometers to monitor the transient response of burning carbonaceous particles.” Review of Scientific Instruments, 1992, 63:3608-3622.
[60] Khatami R, Levendis YA. “On the deduction of single coal particle combustion temperature from three-color optical pyrometry.” Combustion and Flame, 2011, 158(9):1822-1836.

List of Tables:

Table 1 Operating Conditions [41]

Parameters	**Values**
Wall Temperature	1400 K
Temperature of the injected gas	1200 K
Velocity of the gas at the inlet	4.55 cm/s
Initial diameter of the particle	80 µm
Initial temperature of the particle	1200 K
Initial velocity of the particle	15 cm/s

Table 2: Constant parameters used in Eq. 6, [43].

$C_D = a_1 + \frac{a_2}{Re_p} + \frac{a_3}{Re_p^2}$	
$a_1 = 0, a2 = 24.0, a3 = 0$	for $Re_p < 0.1$
$a_1 = 3.69, a2 = 22.73, a3 = 0.0903$	for $0.1 < Re_p < 1.0$
$a_1 = 1.222, a2 = 29.1667, a3 = -3.8889$	for $1.0 < Re_p < 10.0$
$a_1 = 0.6167, a2 = 46.5, a3 = -116.67$	for $10.0 < Re_p < 100.0$
$a_1 = 0.3644, a2 = 98.33, a3 = -2778$	for $100.0 < Re_p < 1000.0$
$a_1 = 0.357, a2 = 148.62, a3 = -4.75 \times 10^4$	for $1000.0 < Re_p < 5000.0$
$a_1 = 0.46, a2 = -490.546, a3 = 5.787 \times 10^5$	for $5000.0 < Re_p < 10000.0$
$a_1 = 0.5191, a2 = -1662.5, a3 = 5.4167 \times 10^6$	for $10000.0 < Re_p < 50000.0$

Table 3: Characteristics of Bagasse Sugarcane residue [41]	
Proximate analysis (received)	
Moisture (%)	4.4
Volatile (%)	83.9
Fixed Carbon (%)	7.7
Ash (%)	4.0
Ultimate analysis (dry basis)	
C	44.3
H	5.7
O	45.5
N	0.2
S	0.07
Ash	4.2
Heating value dry fuel (MJ/kg)	16.3

Table 4 Kinetic constants

Reaction NO.	Kinetic parameters			*d*	*e*	Ref.
	A	*E (J/kmol)*	*b*			
R1	3.12E+05	7.4E+07	-	-	-	[42]
R2	0.002	7.9E+07	0	-	-	[42]
R3	0.052	1.33E+08	0	-	-	[48]
R4	4.4	1.62E+08	1	-	-	[49]
R5	1.33	1.47E+08	1	-	-	[49]
R6	2.119E+11	2.027E+08	-	0.2	1.3	[42]
R7	1.30E+11	1.26E+08	-	0.5	0.5	[51]
R8	5.69E+11	1.465E+08	-	1	0.5	[52]

Figures:

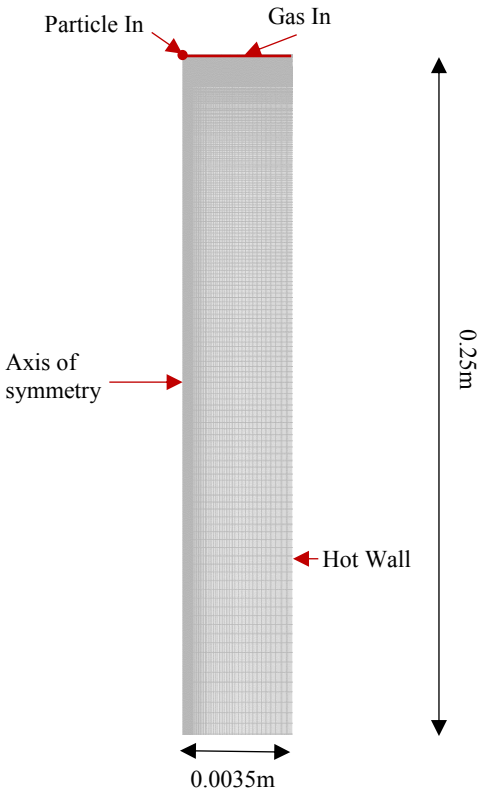

Fig. 1: Schematic view of the computational domain.

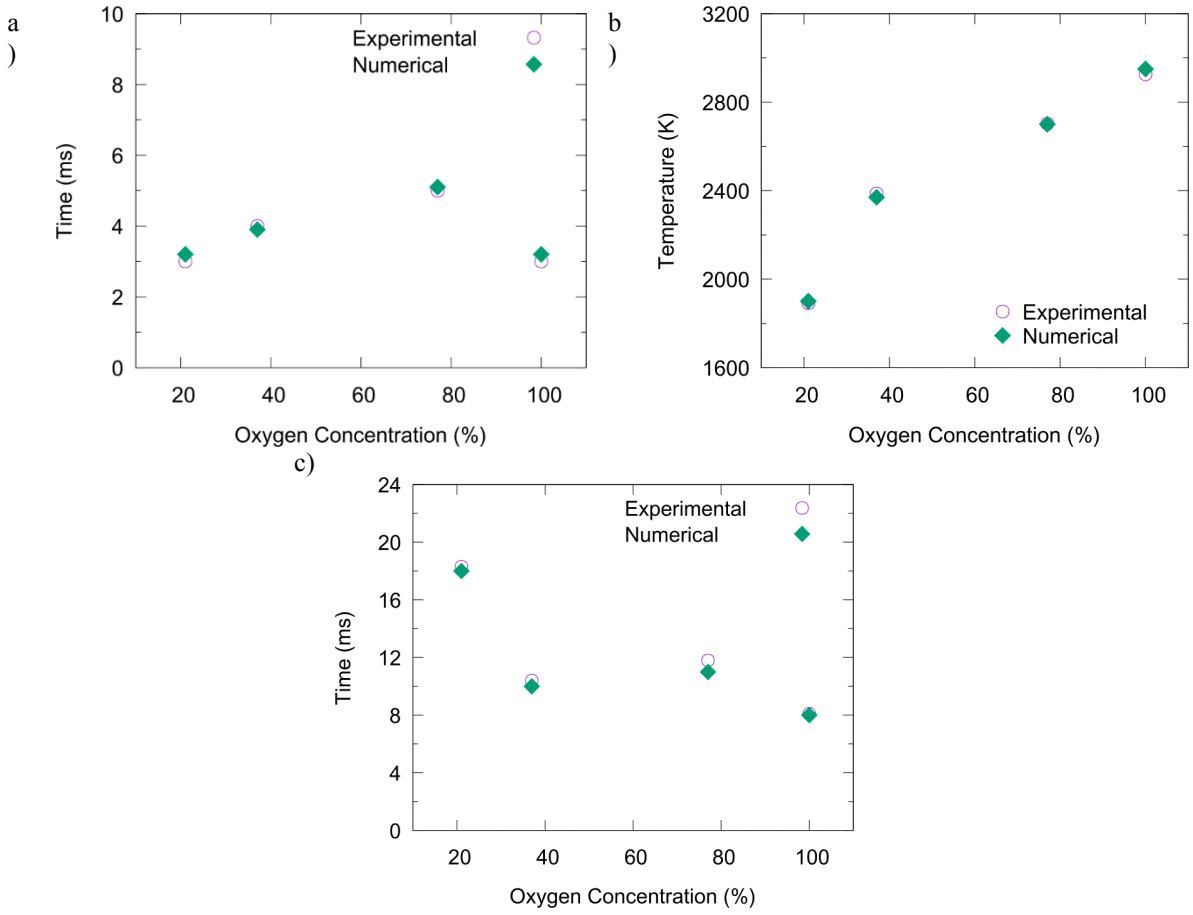

Fig. 2: Comparison between the simulations and experimental measurements [41], a) ignition delay, b) particle maximum temperature, c) particle life time.

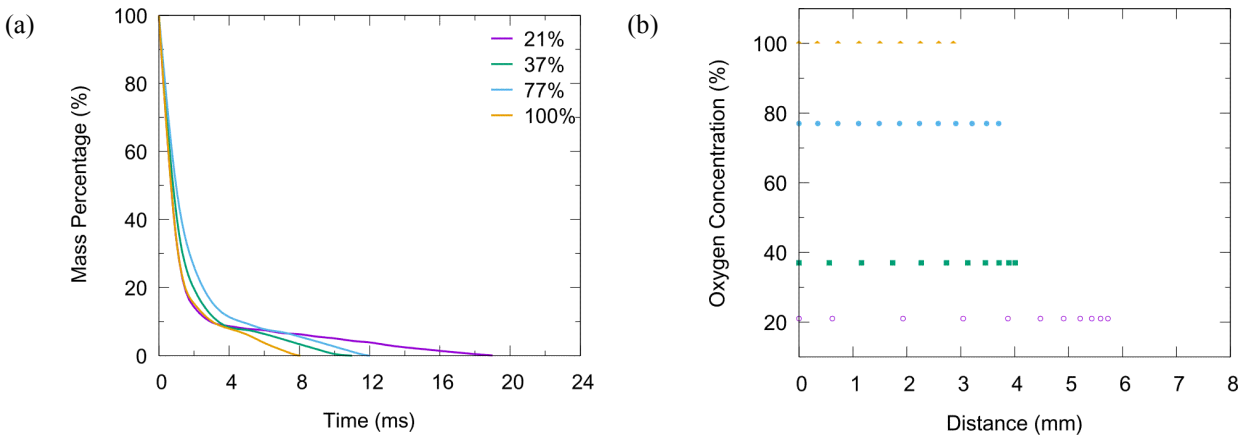

Fig. 3: Illustration of a) percentage of particle mass loss, b) particle position, for different concentration of oxygen.

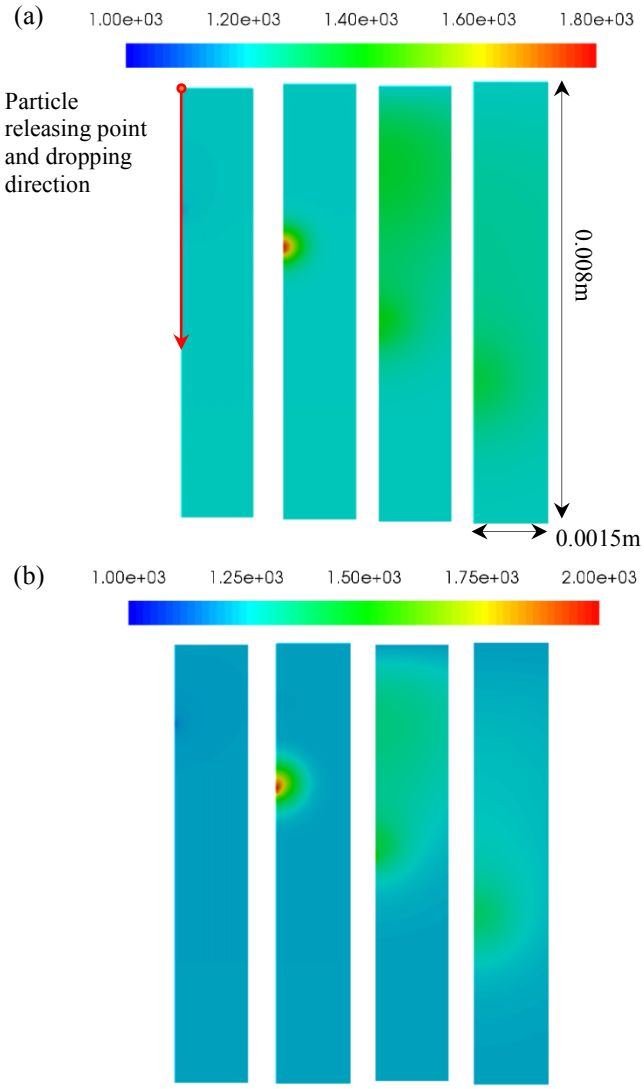

Fig.4: Spatio-temporal distribution of gas temperature, (a) 37% O_2 & 63% N_2 (3ms, 4ms, 7ms, 11ms), (b) 77%$_2$ O_2 & 23% N_2 (3ms, 6ms, 8ms, 12ms).

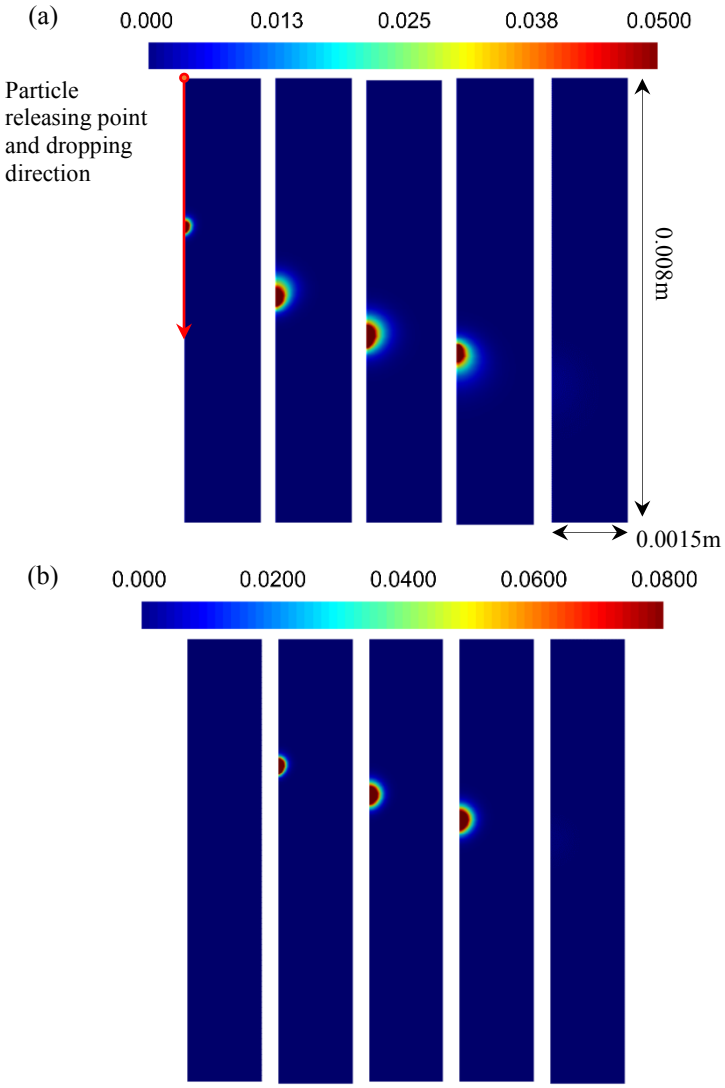

Fig.5: Spatio-temporal distribution of mass fraction of CO, (a) 21% O_2 & 79% N_2 (5ms, 9ms, 13ms, 17ms, 21ms), (b) 77%$_2$ O_2 & 23% N_2 (5ms, 7ms, 9ms, 11ms, 13ms).

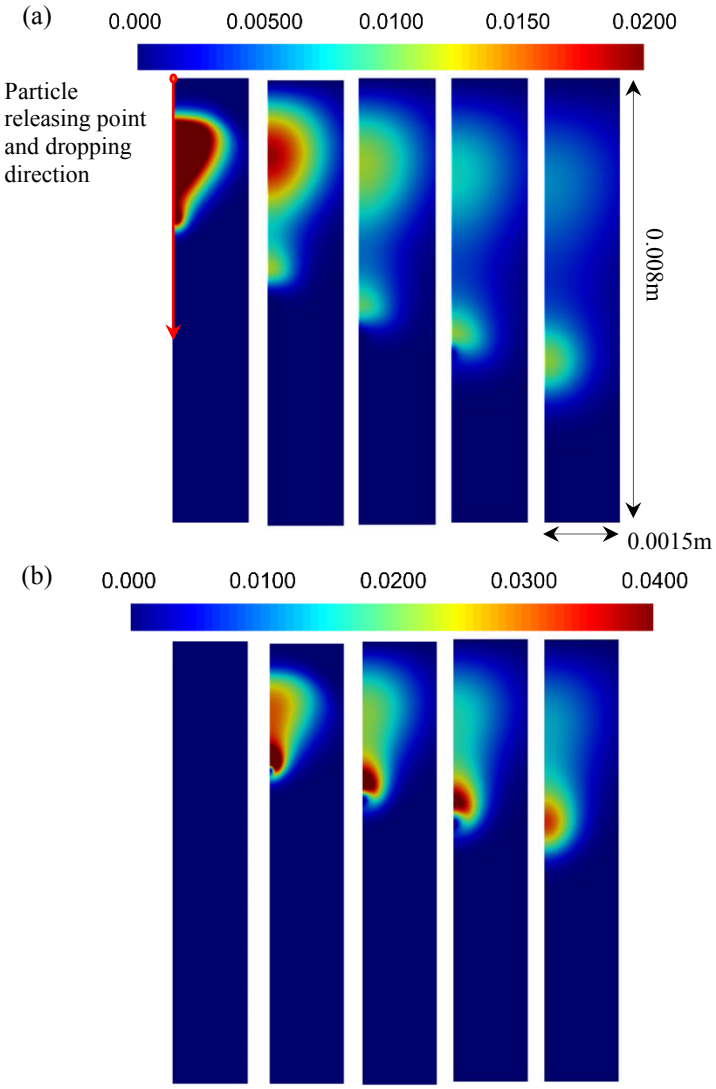

Fig.6: Spatio-temporal distribution of mass fraction of CO_2, (a) 21% O_2 & 79% N_2 (5ms, 9ms, 13ms, 17ms, 21ms), (b) 77%$_2$ O_2 & 23% N_2 (5ms, 7ms, 9ms, 11ms, 13ms).

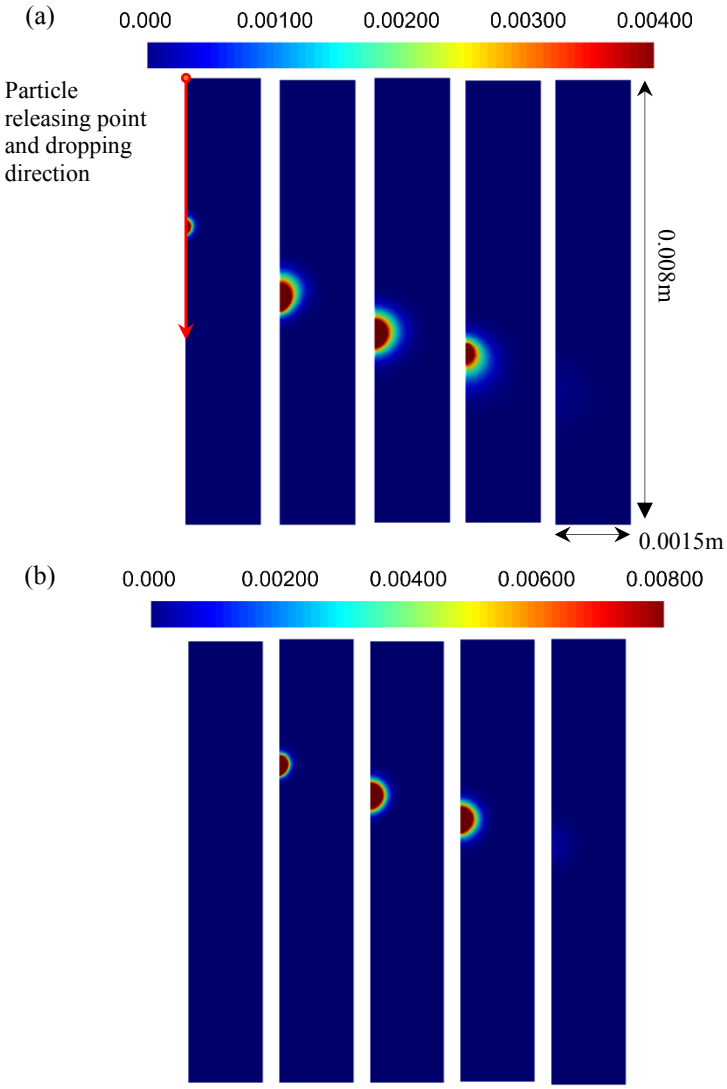

Fig.7: Spatio-temporal distribution of mass fraction of H_2, (a) 21% O_2 & 79% N_2 (5ms, 9ms, 13ms, 17ms, 21ms), (b) 77%$_2$ O_2 & 23% N_2 (5ms, 7ms, 9ms, 11ms, 13ms).

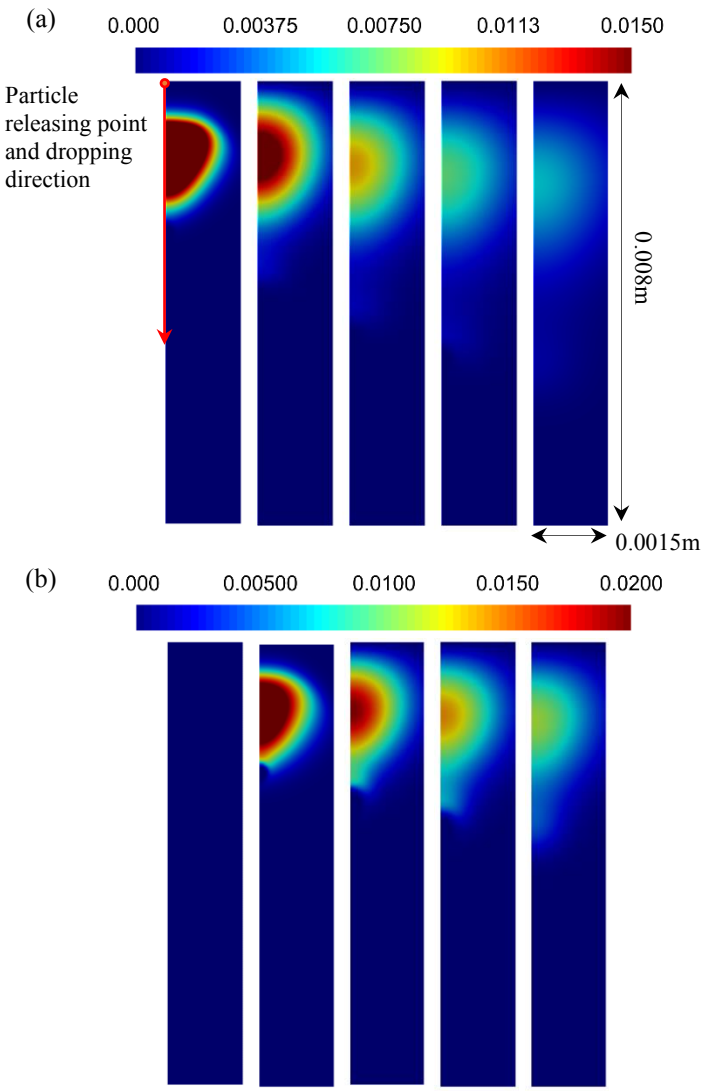

Fig.8: Spatio-temporal distribution of mass fraction of H_2O, (a) 21% O_2 & 79% N_2 (5ms, 9ms, 13ms, 17ms, 21ms), (b) 77%$_2$ O_2 & 23% N_2 (5ms, 7ms, 9ms, 11ms, 13ms).

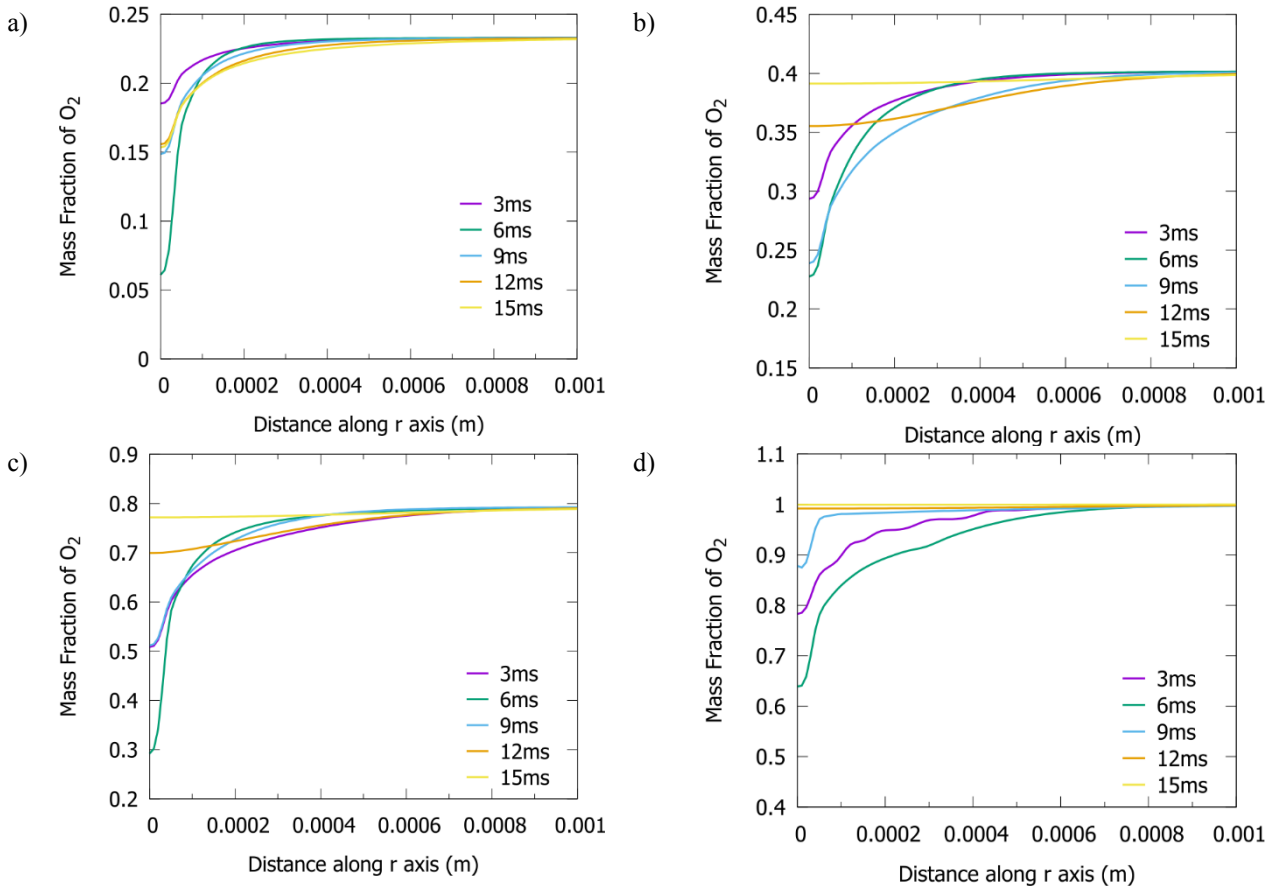

Fig. 9: distribution of oxygen mass fraction along a horizontal line initiating at the particle centre, a) 21% O_2, b) 37% O_2, c) 77% O_2, d)100% O_2 .

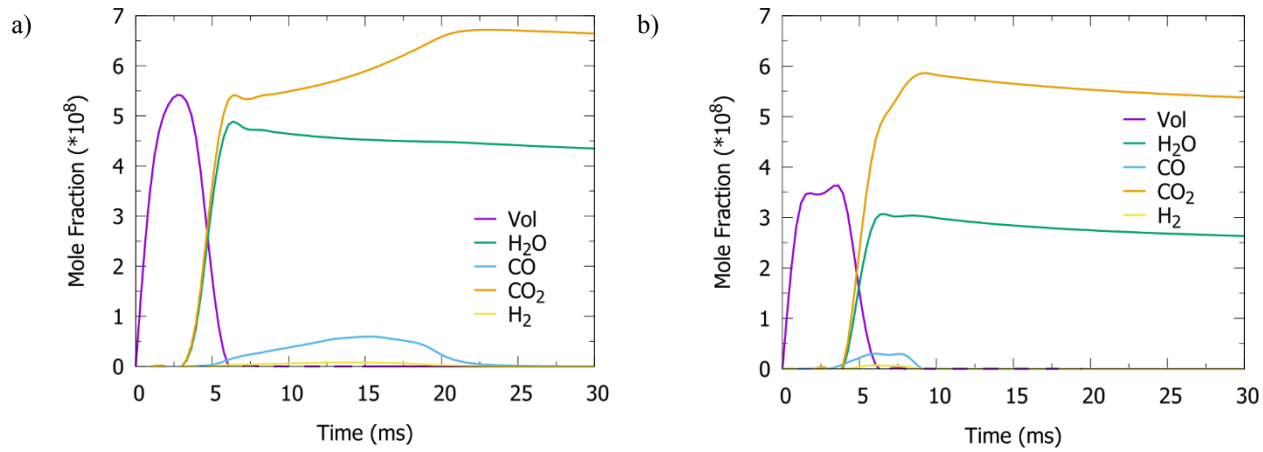

Fig. 10: History of mass-averaged mole fraction of major chemical species a) 21% O_2, b) 100% O_2.

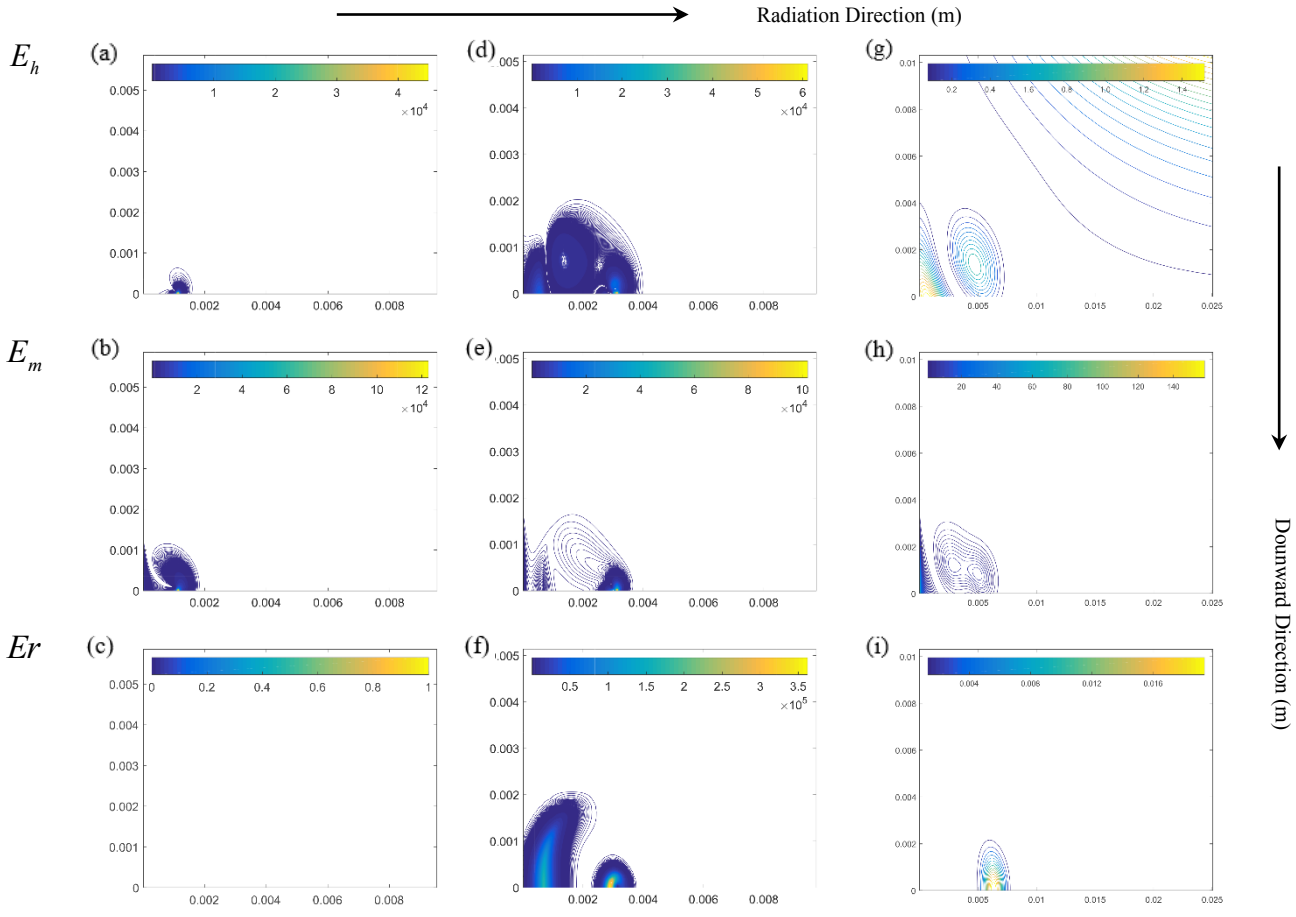

Fig 11: Spatio-temporal evolution of entropy generation rate per unit volume (W/m^2K) under for 37% O_2 & 67% N_2.

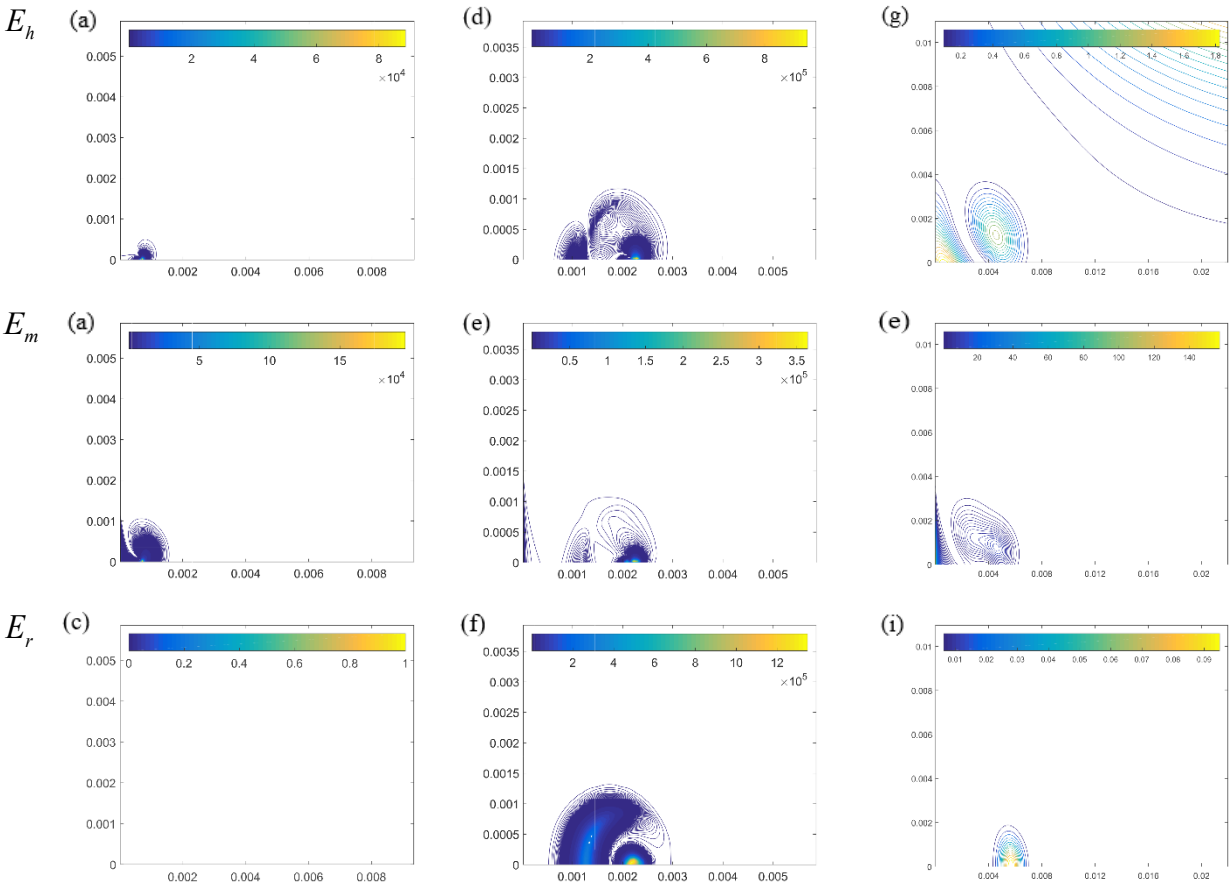

t1=2ms t2=6ms t3=20ms

Fig 12: Spatio-temporal evolution of entropy generation rate per unit volume (W/m^2K) under for 77% O_2 & 23% N_2.

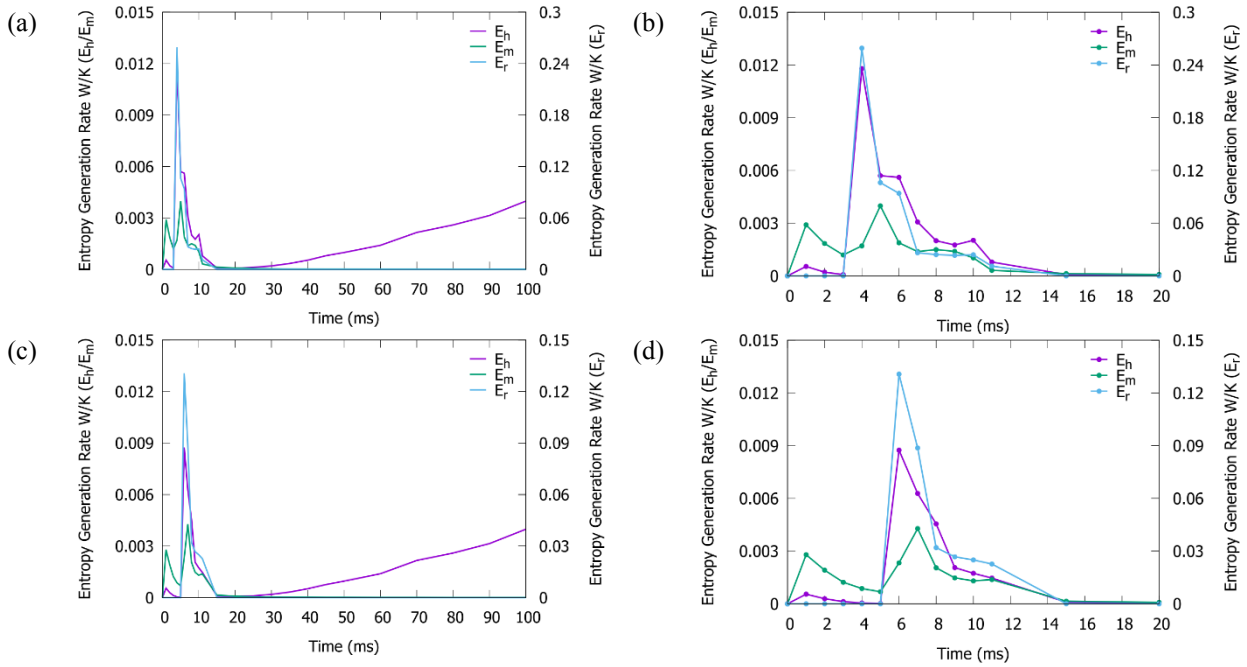

Fig. 13: History of entropy generation by different irreversibilities, a) & b) 37% O_2 & 67% N_2, c) & d) 77% O_2 & 23% N_2. E_H and E_M correspond to the left vertical axes and E_R to be read from the right axes.

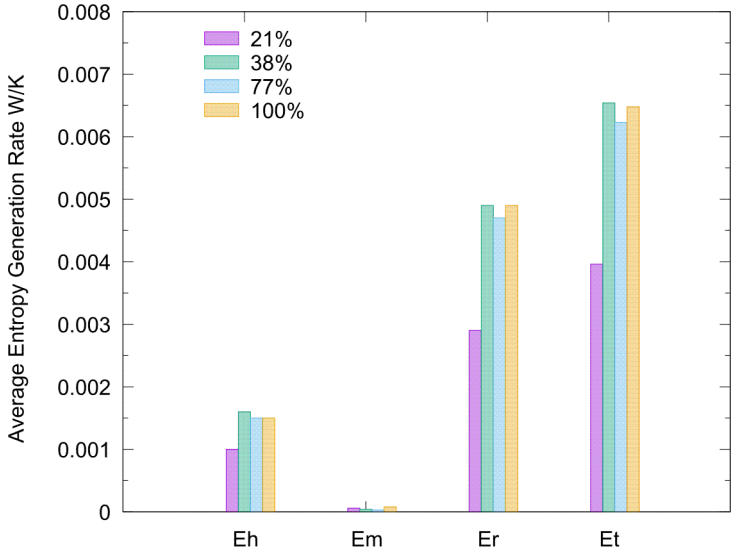

Fig. 14: Total generation of entropy for varying concentrations of oxygen.